AIAA JOURNAL
Vol. 47, No. 8, August 2009

Turbulent Tip Vortex Measurements Using Dual-Plane Stereoscopic Particle Image Velocimetry

Manikandan Ramasamy,* Bradley Johnson,† and J. Gordon Leishman‡
University of Maryland, College Park, Maryland 20742

DOI: 10.2514/1.39202

The formation and evolutionary characteristics of the blade tip vortices generated by a hovering rotor were studied using dual-plane stereoscopic particle image velocimetry. The dual-plane stereoscopic particle image velocimetry technique permitted noninvasive measurement of the three components of the velocity field and the nine components of the velocity gradient tensor, a capability not possible with classical particle image velocimetry. The dual-plane stereoscopic particle image velocimetry method is based on coincident flow measurements made over two differentially spaced laser sheet planes. A polarization-based approach was used in which the two laser sheets were given orthogonal polarizations, with filters and beam-splitting optical cubes placed so that the cameras imaged Mie scattered light from only one or other of the laser sheets. The digital processing of the images used a deformation grid correlation algorithm that was optimized for the high velocity gradient and small-scale turbulent flows found inside the blade tip vortices. High-resolution flow imaging of the vortex sheet in the wake behind the rotor blade, combined with detailed turbulence measurements, revealed the presence of several turbulent flow features during the vortex roll-up process that appear to play an important role in its final evolution. The dual-plane stereoscopic particle image velocimetry measurements also included the fluctuating terms involved in the Reynolds-averaged stress transport equations. The results confirm that an isotropic assumption of turbulence is invalid inside blade tip vortices and that stress should not be represented as a linear function of strain. The dual-plane stereoscopic particle image velocimetry measurements were also compared with velocity and turbulence measurements made using a laser Doppler velocimeter system, with good correlation.

Nomenclature

A	=	rotor disk area, $=\pi R^2$, m^2
c	=	blade chord, m
C_T	=	rotor thrust coefficient, $=T/\rho A\Omega^2 R^2$
i, j, k	=	direction vectors
N_b	=	number of blades
p	=	static pressure, Nm^{-2}
R	=	radius of blade, m
r, θ, z	=	polar coordinate system, m, rad, m
r_c	=	core radius of the tip vortex, m
r_0	=	initial core radius of the tip vortex, m
Re_v	=	vortex Reynolds number, $=\Gamma_v/\nu$
u, v, w	=	velocities in Cartesian coordinates, ms^{-1}
u', v', w'	=	fluctuating velocities in particle image velocimetry coordinates, ms^{-1}
$U_{\rm rms}, V_{\rm rms}, W_{\rm rms}$	=	rms velocities in particle image velocimetry coordinates, ms^{-1}
$\overline{u'v'}$	=	Reynolds shear stress in X, Y plane, m^{2}s^{-2}
$\overline{u'w'}$	=	Reynolds shear stress in X, Z plane, m^{2}s^{-2}
$\overline{v'w'}$	=	Reynolds shear stress in Y, Z plane, m^{2}s^{-2}
$V_{\rm ax}$	=	axial velocity of the tip vortex, ms^{-1}
V_r	=	radial velocity of the tip vortex, ms^{-1}
$V_{\rm tip}$	=	tip speed of blade, ms^{-1}
V_θ	=	swirl velocity of the tip vortex, ms^{-1}
$V_{r\,\rm rms}, V_{\theta\,\rm rms}$	=	rms velocities in polar coordinates, ms^{-1}
X, Y, Z	=	particle image velocimetry coordinate system, m
x, y, z	=	tip vortex Cartesian coordinate system, m
α	=	Lamb's constant, $=1.25643$
$\alpha_{\rm RL}$	=	Ramasamy–Leishman constant, $=0.0655$
Γ_v	=	total vortex circulation, $=2\pi r V_\theta$, m^{2}s^{-1}
δ	=	ratio of apparent to actual kinematic viscosity
δ_{ij}	=	Kronecker delta
ζ	=	wake age, deg
ν	=	kinematic viscosity, m^{2}s^{-1}
ρ	=	air density, kg m^{-3}
σ	=	strain rate, s^{-1}
τ	=	stress, Nm^{-2}
ψ	=	azimuthal position of blade, deg
Ω	=	rotational speed of the rotor, rad.s^{-1}
2-C	=	two-component
3-C	=	three-component

Received 18 June 2008; revision received 4 December 2008; accepted for publication 6 February 2009.

*Currently Research Scientist at University Affiliated Research Center/Aeroflightdynamics Directorate, NASA Ames Research Center, Moffett Field, CA; mani.ramasamy@us.army.mil. Member AIAA.

†Graduate Research Assistant and National Defense Science and Engineering Graduate Fellow; bjo212@umd.edu. Student Member AIAA.

‡Minta Martin Professor of Engineering; leishman@umd.edu. Associate Fellow AIAA.

I. Introduction

DECADES of research have been directed toward gaining an understanding of the complex vortical wakes generated by helicopter rotors (e.g., [1–10]) and assessing the effects of the wake on vehicle performance, unsteady airloads, vibration, and noise levels. Much of the research has been rightfully focused on better understanding the characteristics of the blade tip vortices, which are the dominant features of a helicopter rotor wake (e.g., [11–17]). The tip vortices can remain in the proximity of the rotor for several rotor revolutions, and this can lead to the production of significant unsteady airloads on the blades and to various other problems.

It is, therefore, important to better understand and predict the physics that determine the formation, strength, and trajectories of these tip vortices, so as to develop more consistent and reliable mathematical models that faithfully describe the aerodynamics of the rotor. To this end, no model can be completely successful unless it is able to accurately represent the three-dimensional turbulent flows that are present inside the vortices. Analytical models of tip vortex

evolution have been developed by making several assumptions in solving the Navier–Stokes (N–S) equations, for example, the classical Lamb–Oseen vortex model. These assumptions usually do not completely represent all of the flow physics, and so the resulting models give inaccurate predictions of the core growth and other properties of actual blade tip vortices. Nevertheless, such simplified vortex models and empirical modifications of such [18,19] have formed the basis for models that are today used in many types of the comprehensive rotor simulations [6,20,21].

Predicting rotor wake developments using computational fluid dynamics (CFD) methods based on the N–S equations are steadily on the rise. Direct numerical solution (DNS) of the N–S equations is presently unrealistic for rotor wake problems because of the high computational expense. Much more effort in the CFD field has been focussed toward solving the Reynolds-averaged Navier–Stokes (RANS) equations. RANS methods time average the N–S equations by representing the flow velocity u_i at a point as a combination of a mean component $\bar{u}_i$ and a fluctuating component u_i' as given by the equation

$$u_i = \bar{u}_i + u_i' \tag{1}$$

Using Eq. (1) in the incompressible form of the N–S equations results in the RANS equations, as given by

$$\frac{\mathrm{D}\bar{u}_i}{\mathrm{D}t} = \frac{\partial}{\partial x_j}\left[-\frac{\bar{p}\delta_{ij}}{\rho} + \nu\left(\frac{\partial \bar{u}_i}{\partial x_j} + \frac{\partial \bar{u}_j}{\partial x_i}\right) - \overline{u_i' u_j'}\right] \tag{2}$$

where $\mathrm{D}/\mathrm{D}t$ is the substantial derivative and $\overline{u_i' u_j'}$ are the correlation (or Reynolds shear stress) terms. The overbar in each case represents the time-averaged values.

Time averaging the N–S equations to form the RANS equations bypasses the need to directly compute the high-frequency, small-scale fluctuations caused by turbulent eddies in the flow (i.e., the u_i' and u_j' terms). However, this advantage with the RANS equations is countered by the creation of an additional unknown term, the Reynolds shear stress $\overline{u_i' u_j'}$. This turbulent stress term makes the RANS equations unsolvable unless a closure model is used to rebalance the number of equations and unknowns. This so-called correlation term basically accounts for the effect of velocity fluctuations created by the presence of eddies of different length scales. Therefore, it is vital that any turbulence closure model adopted be consistent with the actual flow physics so as to correctly model the contributions of turbulence to the developing flows.

The objective of the present work was to measure the complex turbulent wake (i.e., both the vortex sheet and the tip vortex) of a small-scale rotor using particle image velocimetry (PIV) and laser Doppler velocimetry (LDV) with high spatial and temporal resolution. These objectives were accomplished by employing: 1) a conventional PIV system using a high-resolution 11 megapixel charge-coupled device (CCD) camera, which provided a great deal of quantitative information on the formation of the tip vortices and the transport of the turbulence between the vortex sheet and the tip vortex, 2) a dual-plane PIV (DPS-PIV) technique, which could simultaneously measure the six in-plane velocity gradients and three out-of-plane velocity gradients needed for understanding the turbulent flows, and 3) a separate, independent set of LDV measurements to compare with and validate the PIV data.

The primary purpose of the present work was to help understand the production, transport, and diffusion of turbulence in both the near- and far-wake of the rotor. The results can be used to validate and improve upon turbulence models and to validate outcomes from RANS flow solvers.

II. Measurement Requirements

Generally, the turbulence characteristics of any one type of flowfield depends on the length scales of the turbulent eddies present in the flow, any time-history effects in the flow, and the influence of *nonlocal* effects such as the presence of a solid boundary. Developing a general turbulence model to include all of these effects for all flow conditions is very challenging and is yet to be achieved. This can be appreciated from the fact that the turbulence fluctuations observed in a free shear flow, for example, are different from those found in a bounded flow. As a result, flow-dependent turbulence models have been customized for a given set of flow conditions. The Johnson–King model, for example, is often used for separated flows [22]. Similarly, the V^2-F model is more suitable for low Reynolds number flows [23].

Because different turbulent models must be developed for different physical problems and types of flows, the models will understandably vary in complexity and in the number of equations and coefficients used in the model. Regardless, every model requires a certain number of closure coefficients (or constants) and damping functions. The simple Prandtl's mixing length model, for example, requires just one constant, whereas the modified Baldwin–Lomax model requires six constants [24]. The frequently used Spalart–Allmaras [25] model contains eight constants and three damping functions, whereas the Baldwin–Barth model contains seven constants, two damping functions, and one additional function for the length scale [26]. The closure coefficients and damping functions have been derived from experimental measurements of free shear or homogenous flows.

Naturally, problems can arise when such turbulence models are applied to more complicated flows, which may involve shock waves or high streamline curvature. It is known, for example, that the high streamline curvature found in tip vortices can suppress the creation of turbulence or even produce rotational stratification of turbulence near the vortex core axis. This is a physical effect that is unaccounted for in turbulence models that are used without modification [27,28]. This behavior can be seen in Fig. 1, which shows a stroboscopic laser light sheet visualization performed in the flowfield of a hovering rotor and targeting the fully formed blade tip vortex. It is apparent that the vortex comprises three main regions: 1) an inner zone with few eddies and little interaction between adjacent fluid layers, 2) a more transitional flow region with turbulent eddies of different scales that become more stratified as they approach the inner zone, and 3) an outer region that is turbulent but free of large eddies.

This zoned representation of the vortex is analogous to the make up of a turbulent boundary layer, which is composed of a viscous sublayer, a logarithmic layer, and an outer freestream flow. Although Van Driest [29,30] used a damping function to model the logarithmic layer, Klebanoff [31] used an intermittency function to represent the turbulent fluctuations from the wall out to the outer freestream flow. Based on a similar concept, Ramasamy and Leishman [32] developed an intermittency function to represent the eddy viscosity variation across a tip vortex, and derived a semiempirical solution for the evolutionary characteristics of turbulent vortices as a function of vortex Reynolds number. The Ramasamy and Leishman (R–L) eddy viscosity model is described by

$$\nu_T = \nu + \mathrm{VIF}\,\alpha_{\mathrm{RL}}^2 |\sigma| \tag{3}$$

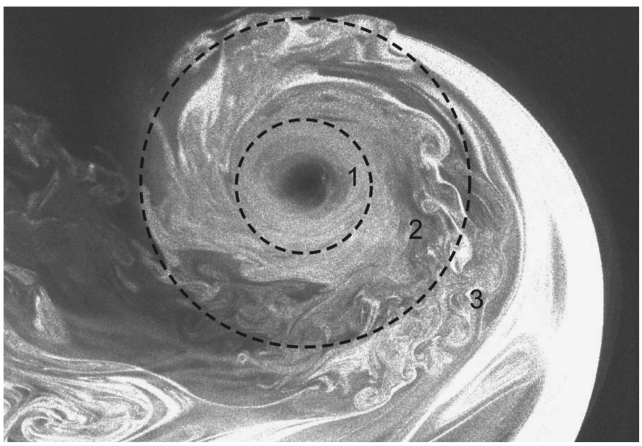

Fig. 1 Laser light sheet flow visualization of a fully developed blade tip vortex where "1" shows the inner zone free of large turbulent eddies, "2" shows a transitional region with eddies of different scales, and "3" shows an outer, essentially potential flow region.

where ν_T is the total viscosity, VIF the so-called vortex intermittency function, and α_{RL} is an empirical constant derived from many vortex flow measurements. This model is based on Prandtl's mixing length hypothesis, but it addresses the effects of rotational stratification through a Richardson number effect [32]. For example, Fig. 2 shows the distribution of the Richardson number inside the tip vortex, which can be defined as the ratio of turbulence produced or consumed inside the vortex to the turbulence produced by the shear. It can be seen that the Ri number decreases quickly from infinity at the center of the vortex and approaches a threshold value. It has been argued [33] that turbulence cannot develop until the value of Ri number falls below this threshold. The R–L eddy viscosity model was based on this idea, and the closure coefficients associated with the model were derived by first finding a mathematical solution to the one-dimensional N–S equations, followed by comparing the Reynolds-number-dependent similarity solution to the induced velocity profiles of the tip vortex.

Further validation of this vortex model (and other models), however, requires careful measurements of turbulence activity inside the tip vortices. It also requires an understanding of how the turbulence contained in the inboard vortex sheet trailed from the blade participates in the tip vortex roll-up process. Understanding this process is difficult because the flow is highly three-dimensional and involves high pressure and velocity gradients. Simple idealizations of the roll-up are inevitably inviscid descriptions and ignore the intricate details of the flow physics. For example, secondary and tertiary vortices are known to form when the viscous nature of the flow couples with the local pressure gradients [34], which results in flow separations from side-edge surfaces of the blade tip. These flow structures continue to evolve over the upper surface of the blade, but they ultimately do merge into one strong vortex downstream of the trailing edge. Furthermore, part of the shear layer from the trailing edge is also entrained into the tip vortex flow. Although the tip vortex appears fully rolled up and largely axisymmetric in the far field [34], modeling the turbulence inside the vortices as they evolve in the flow still depends on faithfully modeling its roll up and in determining accurately its initial strength.

III. Description of Experiment

The present study involved the application of both LDV and PIV techniques. For the PIV, a two-component configuration was first used to analyze the vortex sheet with a high-resolution 11 megapixel CCD camera. This was followed by measurements made using a DPS–PIV system with a pair of 4 megapixel CCD cameras and a single 2 megapixel CCD camera. Because a two-component PIV configuration is well documented, the discussion in this paper is mainly about the issues associated with DPS–PIV technique.

Both of the PIV and LDV measurement techniques used the same seed particles, with an average diameter of 0.22 μm; this particle size was small enough to minimize tracking errors in the wake flow [35].

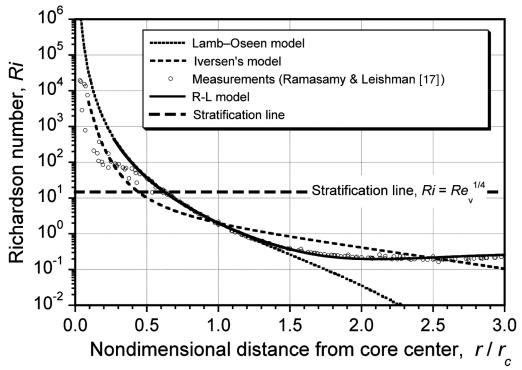

Fig. 2 The variation of the Richardson number across a blade tip vortex suggests that turbulence production will be suppressed in the central core region.

A. Rotor System

A single-bladed rotor operated in hover was used for the measurements. The advantages of the single-blade rotor have been addressed before [36,37]. These include the ability to create and study a helicoidal vortex filament without interference and instability issues caused by other blades and other vortices [36,37]. This allows for the vortex structure to be studied to much older wake ages (i.e., the time since the tip vortex was trailed from the rotor blade in terms of blade position) without the high levels of aperiodicity in the flow that are produced when using multibladed rotors.

The single blade was of rectangular planform, untwisted, with a radius of 406 mm (16 in.) and chord of 44.5 mm (1.752 in.), and was balanced with a counterweight. The blade airfoil section was the NACA 2415 throughout. The rotor tip speed was 89.28 m/s (292.91 ft/s), giving a tip Mach number and chord Reynolds number of 0.26 and 272,000, respectively. The zero-lift angle of the NACA 2415 airfoil is approximately -2 deg at the tip Reynolds number. All the tests were made at an effective blade loading coefficient of $C_T/\sigma \approx 0.064$ using a collective pitch of 4.5 deg (measured from the chord line). The rotational frequency of the rotor was set to 35 Hz ($\Omega = 70\pi$ rad/s).

B. DPS–PIV Setup

DPS–PIV differs from conventional PIV because it can measure all nine components of the velocity gradient tensor and the three velocity components. A conventional, stereoscopic (three-component) PIV system is capable of measuring three components of velocity in a given plane [38–41] but only six of the nine velocity gradient tensor components. The velocity gradient tensor can be written as

$$\nabla V = \begin{bmatrix} \partial u/\partial x & \partial u/\partial y & \partial u/\partial z \\ \partial v/\partial x & \partial v/\partial y & \partial v/\partial z \\ \partial w/\partial x & \partial w/\partial y & \partial w/\partial z \end{bmatrix} \tag{4}$$

Estimating all of the velocity gradients in the out-of-plane direction [i.e., finding the $\partial/\partial z$ terms in Eq. (4)] requires the measurement of three components of velocity in at least two planes that are parallel to each other and are separated by a small spatial distance in the z direction.

1. *DPS–PIV Imaging Arrangement*

The optical setup of the DPS–PIV system is shown in Fig. 3. Two coupled PIV systems are required to simultaneously measure the flow velocities from Mie scattering of the particles passing through both of the laser sheet planes. Three dual Nd:YAG lasers with 110 mJ/pulse were used, the third laser being used to image the flow in regions where the blade casts a shadow, thereby preventing the need to mosaic the resulting images. The DPS–PIV system can be arranged as a combination of two stereoscopic PIV systems [42] or as a combination of one stereoscopic PIV system and one two-component PIV system [43,44]. Although the former combination provides all the three components of velocity in both of the two parallel planes, the latter provides the three components of velocity in one plane and only the in-plane velocities (i.e., two flow components) in the other plane. The out-of-plane velocity is then calculated by using continuity assumptions. This second method provides several advantages over a dual-plane stereoscopic setup, including its simpler configuration and lower cost.

The present setup is shown in Fig. 3. A conventional 2-C PIV configuration (the 2 megapixel camera is labeled as C2 in Fig. 3) is used to measure two components of flow velocity in one plane, and a stereo setup (a pair of 4 megapixel cameras labeled C1 and C3 in Fig. 3) is used to measure the three flow velocity components in the second plane. The stereo cameras satisfied the Scheimpflug condition for PIV imaging. The resulting velocity fields that are measured in the two planes (Fig. 4) can then be analyzed to determine eight out of nine components of the velocity gradient tensor. The ninth velocity gradient ($\partial w/\partial z$) can be estimated by using the incompressible form of the continuity equation.

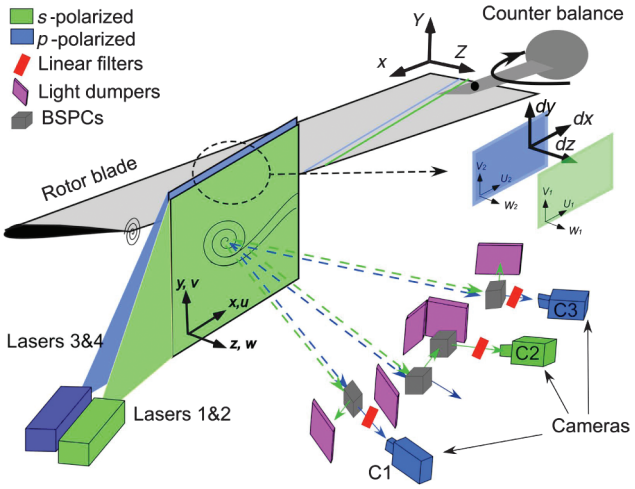

a) Schematic

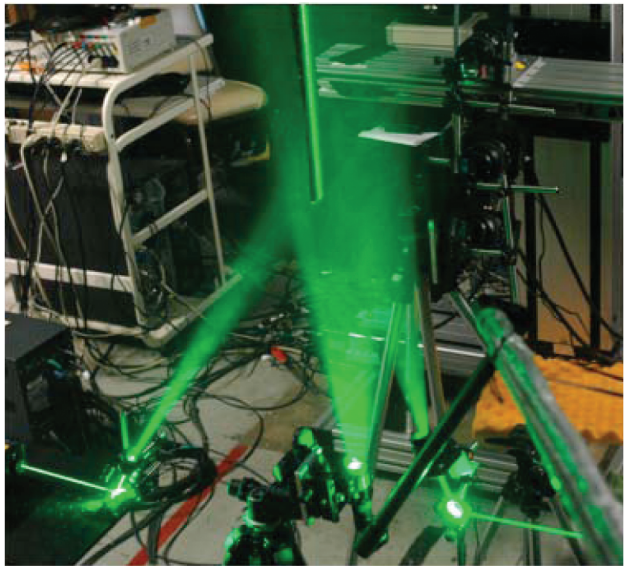

b) Three dual Nd-YAG lasers illuminating the flow

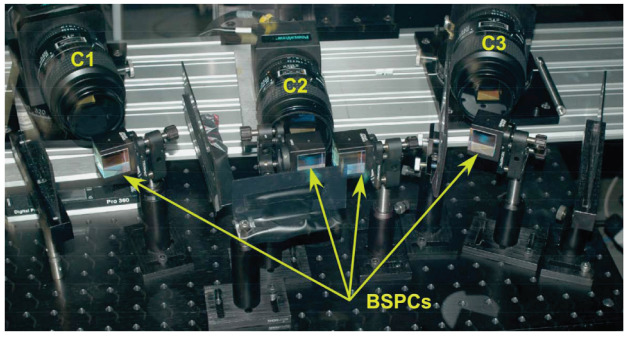

c) Close-up of CCD cameras and beam splitting cubes

Fig. 3 Schematic and photographs of the DPS–PIV system as used for the rotor wake studies.

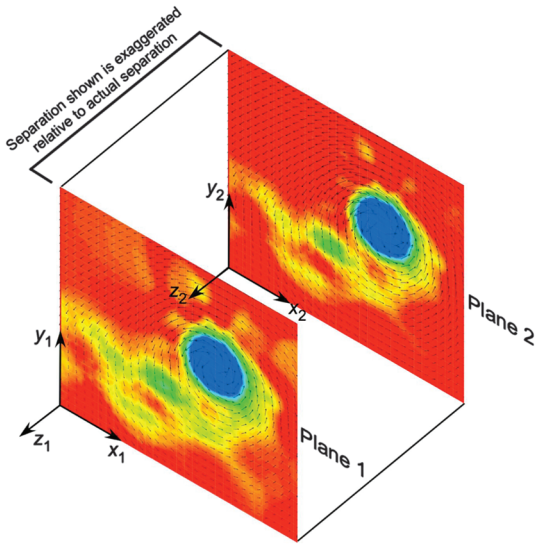

Fig. 4 Typical instantaneous velocity fields measured using DPS–PIV. Interplane separation is exaggerated; actual plane separation is much smaller than the vector-to-vector spacing within each plane.

To ensure the correctness of these velocity gradient measurements several precautions have to be taken. In terms of the setup procedures, the two laser light sheet planes must be both parallel and adjacent (ideally just a small distance apart) to each other. This was achieved by initially aligning both the laser light sheets so that they were coplanar before moving the second laser light sheet using a micrometer-controlled linear stage. Additionally, the two Nd:YAG lasers must be synchronized, not only with each other but also with both sets of cameras and to the rotational frequency of the rotor.

For the present experiment, each laser pair (i.e., lasers 1 and 2 and lasers 3 and 4 shown in Fig. 3) delivers two pulses of laser light with a pulse separation time of 2 μs. The first laser pulse from the green pair (laser 1) must be synchronized with the first laser pulse from the blue pair (laser 3), and the same approach is conducted for the second laser pulse from each laser pair (lasers 2 and 4). Each of the three cameras must then be synchronized with the lasers (i.e., the first particle pair image in each plane is captured upon the firing of lasers 1 and 3 and the second image in each plane is captured during the firing of lasers 2 and 4).

There are several challenges with simultaneous measurements in spatially adjacent, parallel laser planes, mainly resulting from crosstalk between the cameras. Crosstalk, which manifests as Mie scattering from both illuminated laser planes (because the sheets are separated by only a few millimeters), can occur because each camera has a finite depth of field. If any camera images reflections from seed particles in both planes, not only will its planar velocity map be erroneous after PIV processing, but the comparison between the velocity map in the first plane with that of the second plane (which is needed to calculate velocity gradients in the z direction) would be meaningless. This problem is heightened by the need to have the intensity of each laser set to high energy levels so that sufficient Mie scattering can be captured by all of the cameras with similar levels of intensity.

To guarantee that each respective set of cameras only images the flow in its designated laser plane, the special optical setup shown in Fig. 3 was used. The purpose was to split the polarizations of the two respective laser pairs (lasers 1 and 2 are s-polarized and lasers 3 and 4 are p-polarized) and then to use appropriate filters and beam-splitting optical cubes placed in front of each camera to guarantee that they only visualize one type of polarized light. In the present setup, the middle 2-C camera (C2) was tuned to the s-polarization of lasers 1 and 2, and the stereo cameras (C1 and C3) were tuned to the p-polarized light lasers from 3 and 4. An in-situ calibration procedure was used to determine the relationships between the two-dimensional image planes and three-dimensional object fields for both position mapping and three-component velocity reconstruction.

Figure 3 shows how the Mie scattered blue (p-polarized) and green (s-polarized) light come from each respective laser sheet. One beam-splitting cube in front of the 2-C camera initially sees both sets of scattered images and allows the p-polarized blue light to pass directly through but redirects the s-polarized green light to a second beam-splitting cube. The second cube simply acts as 45 deg mirror by redirecting the s-polarized light into the camera. A linear filter over the lens acts as a final buffer against any stray p-polarized light. Each

stereo camera also has one beam-splitting cube placed in front of it. This redirects the *s*-polarized light into separate light dumps adjacent to the cubes and allows the *p*-polarized blue light to pass through to the camera lens. Each stereo camera has a linear filter over the lens (oriented at a different angle than that of the 2-C camera) to act as a final buffer against any *s*-polarized light. Final verification of the working condition of the optical set up was made before measurements were started to ensure that the cameras image only Mie scattering from their designated lasers (i.e., there was no image crosstalk).

Another challenge with DPS–PIV involves the need to make coincident flow measurements in each image plane. Even after optically separating the two PIV systems, care has to be taken to ensure that both systems are synchronized with each other so that the flow is measured coincidently over each laser plane. This synchronization will guarantee that the turbulence measurements will be derived from exactly the same flow features.

2. DPS–PIV Particle Image Processing

The digital processing of the acquired images was performed using commercially available software (TSI InSight) that included a deformation grid correlation algorithm (see [45]). This is a processing technique well optimized for the high-velocity gradient flows found inside blade tip vortices. The interrogation window size was chosen in such a way that the images from both the cameras were resolved to approximately the same spatial resolution to allow measurements to be made of the velocity gradients in the out-of-plane direction.

The steps involved in using this correlation algorithm are shown in Fig. 5. The procedure begins with the correlation of an interrogation window of a defined size (say, 64×64), which is the first iteration. Once the mean displacement of that region is estimated, the interrogation window of the displaced image is moved by integer pixel values for better correlation in the second iteration. This third iteration starts by moving the interrogation window of the displaced image by subpixel values based on the displacement estimated from the second iteration. Following this, the interrogation window is sheared twice (for integer and subpixel values) based on the velocity magnitudes from the neighboring nodes, before performing the fourth and fifth iteration, respectively. The uncertainties associated with calibration, image capture, and processing of images are explained in detail in [46].

Once the velocity is estimated after these five iterations, the window is split into four equal windows (of size 32×32). These windows are moved by the average displacement estimated from the final iteration (using a window size of 64×64) before starting the first iteration at this resolution. This procedure can be continued until the resolution required to resolve the flowfield is reached. The second interrogation window is deformed until the particles remain at the same location after the correlation.

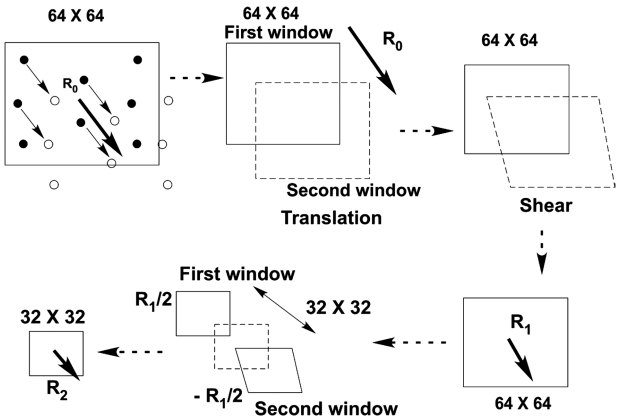

Fig. 5 Schematic of the steps involved in the deformation grid correlation.

3. DPS–PIV Calibration

DPS–PIV imaging requires a calibration process to incorporate the registration of the cameras and their mapping from the object plane onto the image plane to correct for distortions from variable magnification across the image. For the present system, the single camera and stereo camera pair were mapped in the usual way for any single/stereo PIV system, followed by the additional step mapping of the cameras to a single reference frame.

A nonlinear mapping function was created from images of a dual-plane calibration target. This precision calibration target was made from regular grid of white dots on a black background. The resulting mapping function accounts for the distortion and provides the third out-of-plane velocity component. The calibration target was mounted on a micrometer-controlled translation stage. A fiducial reference point on the target defined the origin for all of the calibration images.

C. LDV System

A fiber-optic based LDV system was used to make three-component velocity measurements. To reduce the effective size of the probe volume visible to the receiving optics, the off-axis backscatter technique was used, as described in Martin et al. [47]. This technique spatially filters the effective length of the LDV probe volume on all three channels. Spatial coincidence of the three probe volumes (six beams) and two receiving fibers was ensured to within a 15 μm radius using an alignment technique [47] with a laser beam profiler.

Alignment is critical for three-component LDV systems because this determines the spatial resolution of the LDV probe volume. In the present case, the resulting LDV probe volume was measured using the profiler to be an ellipsoid of dimensions 80 by 150 μm, which is about 3% of the maximum blade thickness or 0.5% of the blade chord. A coincidence window of 80 μs was used to ensure that the same set of particles provided all the three components of the flow velocity. The velocities were then converted into orthogonal components based on measurements of the beam crossing angles.

Each measurement was phase resolved with respect to the rotating blade by using a rotary encoder, which tagged each data point with a time stamp. The temporal phase resolution of the encoder was 0.1 deg, but the measurements were averaged into 1 deg bins [47]. Over 20,000 samples were obtained at each point in the flow, helping to establish the sample size requirement for the statistical convergence of turbulence measurements made inside the tip vortices.

IV. Results and Discussion

The results are discussed in the three categories in which they were measured and analyzed, namely: 1) high-resolution studies of the vortex sheet and the formation of the blade tip vortices, 2) the mean flow characteristics of the tip vortices such as their swirl and axial velocity profiles, and 3) the turbulence characteristics of the tip vortices. It should be noted that the measurements of the vortex sheet and tip vortex roll up were conducted using the 11 megapixel camera, whereas the remainder of the results were obtained using the previously described DPS–PIV system and LDV techniques. The coordinates (and the sign convention) that were used are shown in Fig. 6.

A. Vortex Sheet and Tip Vortex Formation

Figure 7 shows the schematic of the experimental set up used for the high-resolution 2-C PIV measurements. The laser sheet was aligned along the span of the rotor blade at its reference azimuth location, and the 11 megapixel CCD camera was aligned with its optical axis being orthogonal to the laser light sheet.

An instantaneous PIV velocity vector map obtained at 2 deg wake age is shown in Fig. 8. The color contour is the streamwise vorticity, and only every fourth velocity vector is shown to avoid image congestion. This image reveals the complex turbulent flow pattern

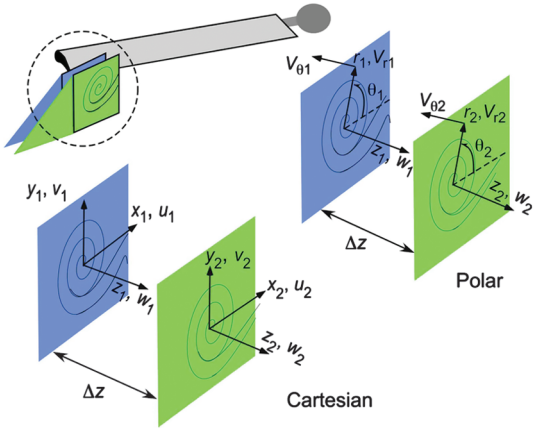

Fig. 6 Schematic showing the coordinate systems used for the present experiments.

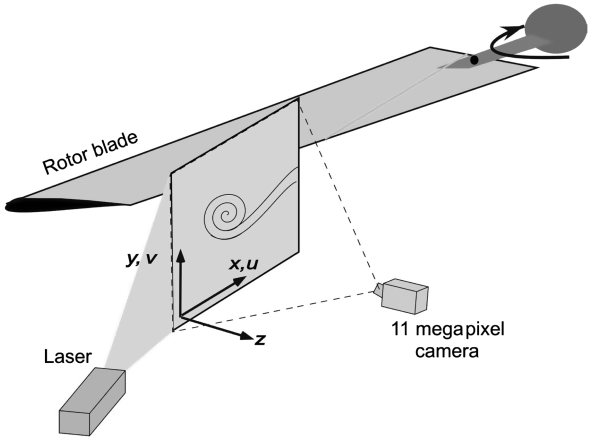

Fig. 7 Experimental setup and targeting used for high-resolution two-component PIV with the 11 megapixel CCD camera.

inside the near wake and clearly shows the flow interactions between the tip vortex the inboard turbulent vortex sheet.

Several observations can be made here. First, the instantaneous vector map (Fig. 8) shows not only the tip vortex forming behind the blade, but also a chain of counter-rotating trailed vortices that are clearly intertwined with one another and with the tip vortex. Notice the interwoven red and blue vorticity contours, which represent clockwise and counterclockwise rotation, respectively. Commonly known as Taylor–Görtler (T–G) vortices [48], these counter-rotating flow structures were present in the wake trailed along the entire span

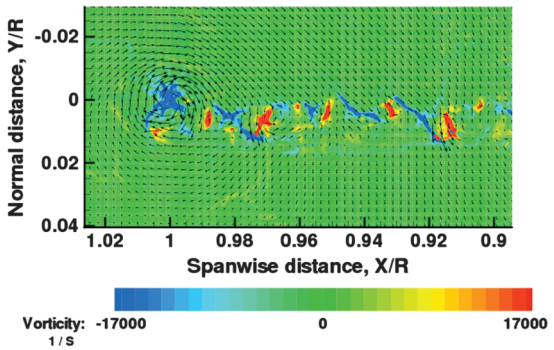

Fig. 8 The presence of Taylor–Görtler vortices in the vortex sheet trailing behind the rotor blade at 2 deg of wake age shows up in the measured velocity and vorticity fields.

of the blade. The presence of the T–G vortical pairs can be attributed to the streamline curvature of the boundary layer on the blade [49].

Various sections of the flowfield measured along the span of the blade are shown in a close-up view in Figs. 9 and 10 and clearly identify the tip vortex and the presence of the T–G vortices, respectively. The T–G vortices are unsteady (aperiodic), showing that the vortical sheet behind the blade and its participation in the roll-up of the tip vortex even at early wake ages is already a turbulent process.

The effects of the aperiodicity in the flow behind the blade are shown in Fig. 11, which was obtained by making a horizontal cut through the center of the tip vortex and along the entire span of the vortex sheet. The results include measurements from the instantaneous vector map and from a phase-averaged vector map, the latter of which was obtained by the simple averaging of

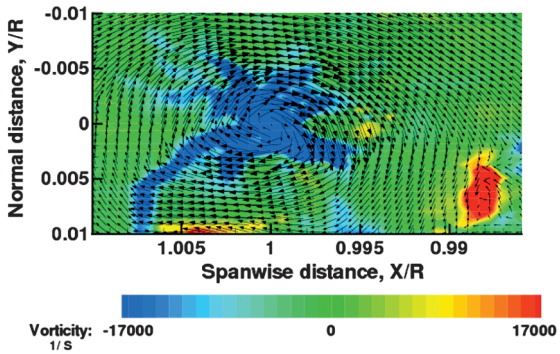

Fig. 9 Close-up of the forming tip vortex at 2 deg of wake age in terms of its initial velocity and vorticity.

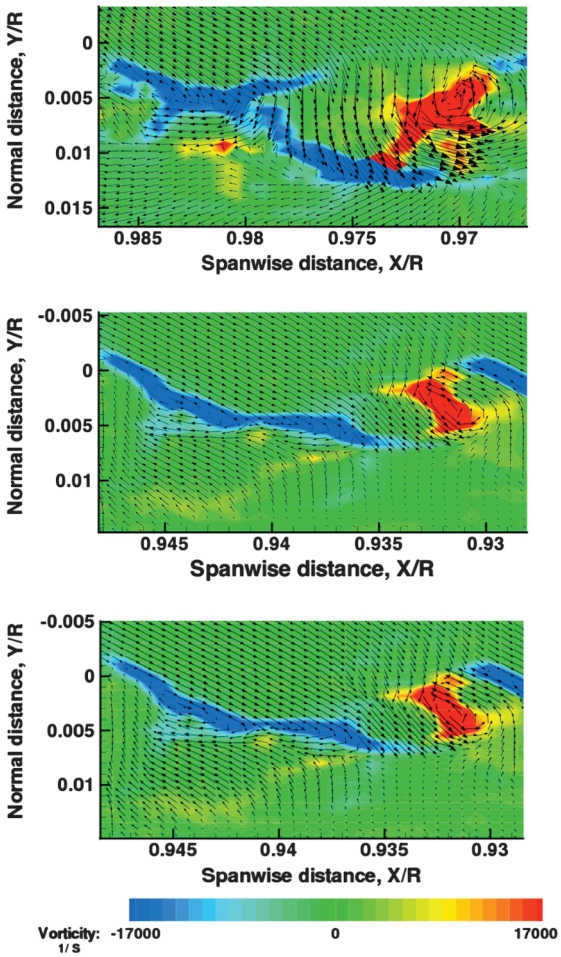

Fig. 10 Details of the velocity and vorticity at the tip vortex and various segments of the inner vortex sheet at 2 deg of wake age.

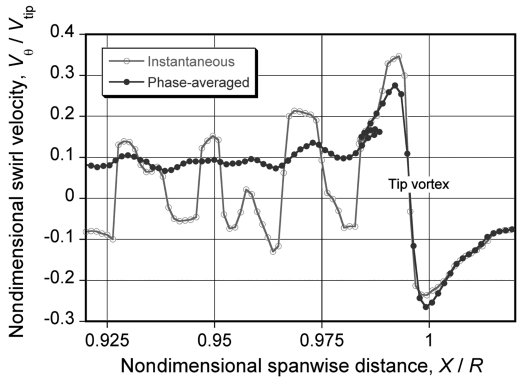

Fig. 11 Clean signatures of the T–G vortex pairs can be seen in the instantaneous flowfield vector maps at 2 deg of wake age but are less apparent in the phase-averaged results.

1000 instantaneous velocity vector maps. It can be seen that the instantaneous swirl velocity profile shows velocity fluctuations that arise from the T–G vortex pairs, whereas the phase-averaging process all but eliminates the features of the turbulent flow. The aperiodic nature of the vortex pairs means that they do not maintain the same spatial location from one phase-resolved measurement to the next. Consequently, their turbulent flow signatures are smeared through the phase-averaging process. Nevertheless, it is these type of small-scale (or smaller), high-frequency aerodynamic structures that contribute to the initial turbulence fluctuations found in the wake flow behind the blade. These fluctuations, when combined with the high velocity gradients found in the tip vortices, play a substantial role in the final roll up of the tip vortices.

B. Tip Vortex Properties

Although the small-scale turbulent vortices in the inboard vortex sheet play some role in defining the turbulence scales in the near downstream wake of the blade, the most dominant flow structure behind the blade is the tip vortex. Therefore, it is important to measure both the mean and turbulent quantities inside the tip vortices and to do so as a function of time as they age in the downstream wake.

1. *Aperiodicity Correction*

Making the distinction between mean and turbulent velocities in the tip vortex is complicated by the fact that the wake becomes more aperiodic as it ages. Even in hover, it is well known that the convecting vortex filaments develop various types of self-induced and mutually induced instabilities and wake modes [37,50] resulting from their interactions with each other. This causes the spatial locations of the tip vortices to change slightly from one rotor revolution to the next, and so the effect appears as an aperiodicity or a "wandering" of the vortex center relative to a mean position in successive PIV images. Unless this aperiodicity effect in the flow is properly and accurately corrected for, it will manifest as incorrect measurements of the turbulent flow components based on Eq. (1).

To give accurate mean flow velocities, the positions of the vortices first have to be colocated such that the center of each vortex is aligned with one another. This guarantees that the individual mean velocities at a point in the flow are calculated based on spatial locations with respect to a defined tip vortex "center" and are not based on its unadjusted spatial location with respect to the image boundaries. The helicity-based aperiodicity bias correction procedure was used in the present study [38]. Mean and turbulence measurements were made from 1000 instantaneous velocity vector maps, and colocating them such that the point of maximum helicity (i.e., $\omega_z \cdot w$) coincided in each of the instantaneous vector maps before the phase-averaging occurred. Only after applying the conditional helicity phase-averaging technique can accurate mean flow properties be estimated. Included in [38] is a detailed analysis that justifies the use of helicity as the ideal tip vortex parameter to use for aperiodicity corrections.

2. *Mean Flow Characteristics of Tip Vortices*

The swirl and axial velocity distributions are shown in Fig. 12 and were determined from the measured data by making horizontal cuts across the vortex. The classical signature of the swirl velocity distribution can be seen here, with the peak swirl velocity continuously decreasing with increasing in wake age.

Measurements of the mean axial velocity at the earliest wake age of 2 deg showed an axial velocity deficit of 75% of the blade tip speed. This component reduced quickly to about 45% of tip speed within just 2 deg of wake age. However, further reduction in the mean axial velocity occurred much more slowly, and the peak value remained near 30% even after 60 deg of wake age. Such high values of axial velocity deficit at the centerline of the tip vortices have been previously reported in [51].

One important derived parameter from these measurements is the viscous core radius of the vortex, which is usually assumed to be the distance between its center (point of maximum helicity) and the radial location at which the maximum swirl velocity occurs. In the present study, the core size was determined using a two-step process. First, a horizontal cut was made across the tip vortex (in a direction along the span of the blade) followed by a vertical cut (in a direction normal to the blade span). The radial locations at which the swirl velocity reached a maximum value on these cuts were then averaged to estimate the core radius. This procedure gives good estimates of the vortex cores for further analysis [38], including those for development of core growth models [19].

The core sizes measured with the DPS–PIV system at various wake ages are shown in Fig. 13, along with measurements made using LDV. All of the measurements were normalized using blade chord. The plot also shows the core growth estimated from Squire's

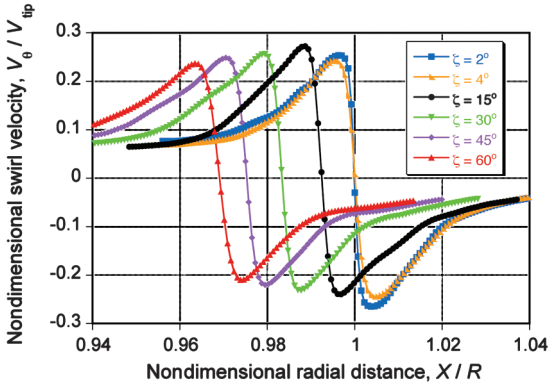

a) Swirl velocity

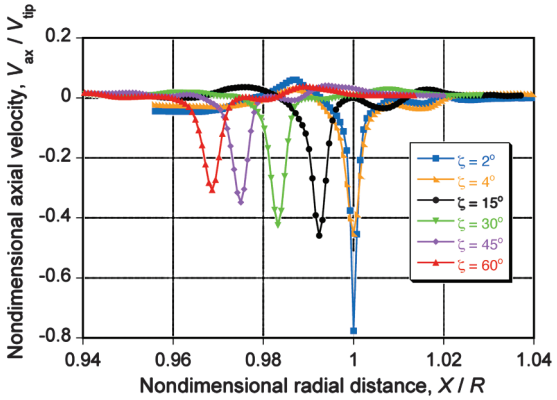

b) Axial velocity

Fig. 12 Normalized swirl and axial velocity distribution at various wake ages.

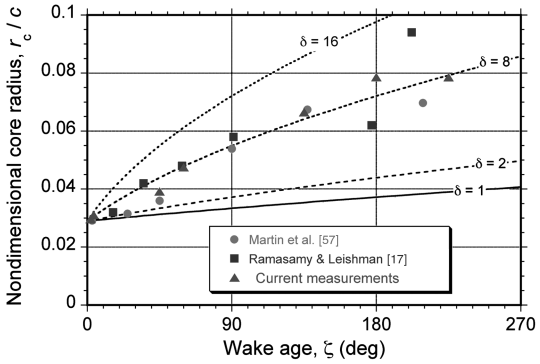

Fig. 13 Core growth characteristics of the blade tip vortices as a function of wake age.

model [52] as modified by Bhagwat and Leishman [19], which is given by

$$r_c(\zeta) = \sqrt{r_0^2 + 4\alpha\nu\delta\left(\frac{\zeta}{\Omega}\right)} \tag{5}$$

Increasing the value of δ basically means that the average turbulence level of the flow inside the tip vortex is increased, which produces more mixing and faster radial diffusion of vorticity and results in a higher average core growth rate with time. It can be seen that the present measurements follow closely the $\delta = 8$ curve.

3. *Velocity Gradients*

The corrected mean flow measurements allow for accurate measurements of all nine velocity gradients in the three flow directions. Figure 14 shows the nine gradients measured at a wake age of 12 deg. The circles marked on each plot represents the average

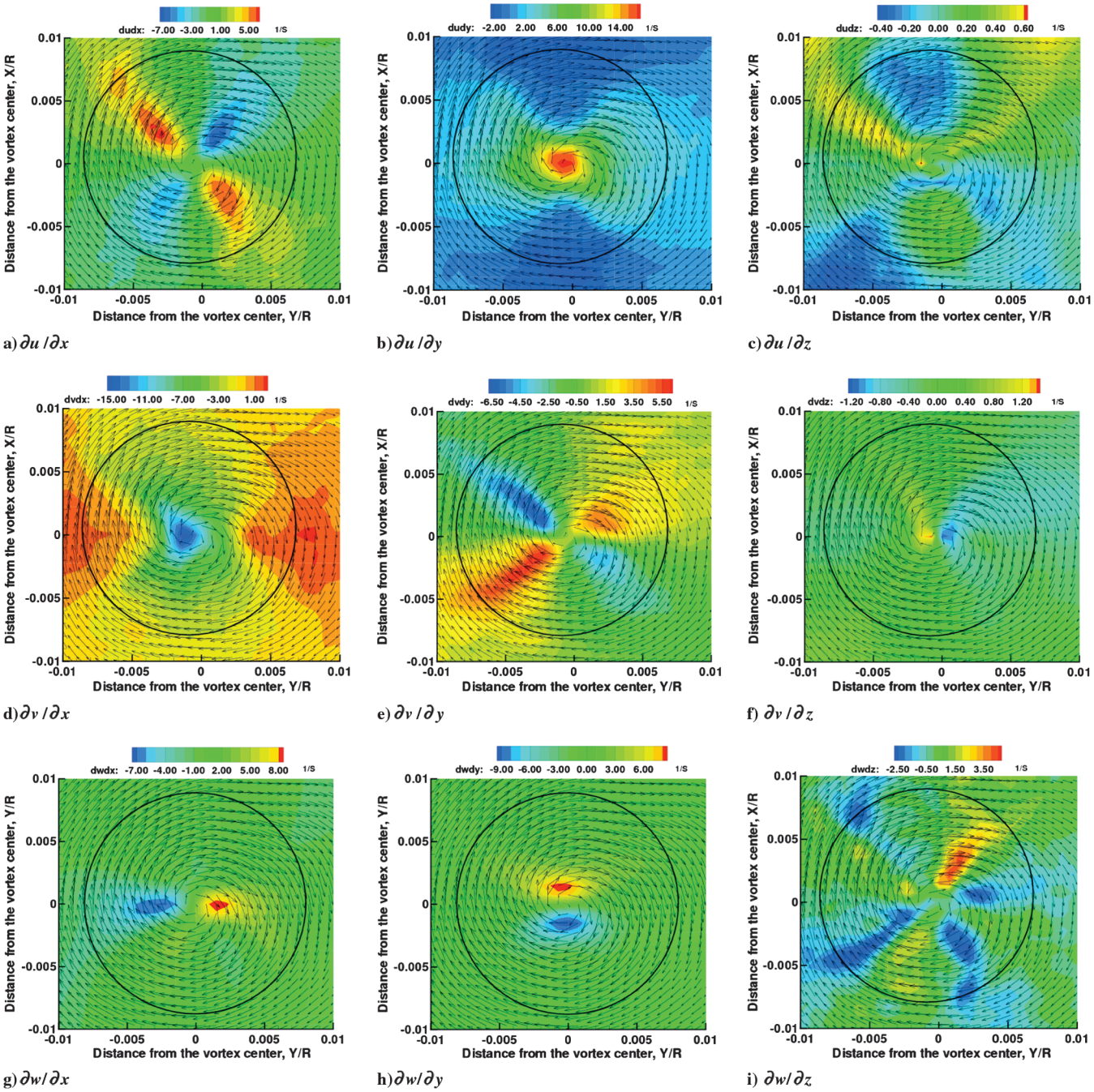

a) $\partial u/\partial x$ b) $\partial u/\partial y$ c) $\partial u/\partial z$

d) $\partial v/\partial x$ e) $\partial v/\partial y$ f) $\partial v/\partial z$

g) $\partial w/\partial x$ h) $\partial w/\partial y$ i) $\partial w/\partial z$

Fig. 14 DPS–PIV measurements of the nine velocity gradients inside the tip vortex core at a wake age of 12 deg.

core size of the tip vortex. As mentioned previously, the value of the ninth gradient $\partial w/\partial z$ was obtained by using the incompressible form of the continuity equation.

It should be noted that not only do all these gradients have different orders of magnitude, but their distributions throughout the vortex flow are also different. The presence of the lobed patterns shown in Fig. 14 are a result of analyzing rotationally coherent flow structures in terms of Cartesian coordinates. On comparing the gradients, both the $\partial u/\partial y$ and $\partial v/\partial x$ components were found to be at a maximum near the vortex center, albeit with opposite signs. Their peak values were also significantly higher than for all of the other velocity gradients, followed by the $\partial w/\partial x$ and $\partial w/\partial y$ terms of which higher magnitudes can be explained by the steep rise in the axial velocity deficit within the viscous core. The $\partial w/\partial y$ and $\partial w/\partial x$ gradients predictably form a two-lobed pattern of opposite sign about the vortex center, mainly because the axial velocity deficit should increase when moving radially inward toward the vortex axis, and decrease when moving radially outward.

The other in-plane velocity gradients (i.e., the $\partial u/\partial x$ and $\partial v/\partial y$ terms) showed four-lobed patterns that were approximately at 45 deg to the x-y coordinate axes. Specifically, the $\partial u/\partial x$ component showed negative lobes at 45 and 225 deg, and positive lobes at 135 and 315 deg. The pattern developed in the $\partial v/\partial y$ gradient was offset from that in $\partial u/\partial x$ by 90 deg. As a result, their sum (which is the ninth velocity gradient, $\partial w/\partial z$) will be relatively small. Notice, the positive lobes in $\partial u/\partial x$ are added to the negative lobes in the $\partial u/\partial x$ component, and vice versa.

For the other streamwise gradients of the in-plane velocities (i.e., $\partial u/\partial z$ and $\partial v/\partial z$), a two-lobed pattern should be expected. Based on the coordinate system followed in this work (Fig. 6), the $\partial u/\partial z$ term is negative on the lobe aligned with the positive y axis and positive on the lobe aligned with the negative y axis. In turn, the swirl velocity gradient $\partial V_\theta/\partial z$ will be negative (z is positive streamwise) at all points inside the vortex core, indicating a reduction in the swirl flow inside the tip vortices. This gradient can be expected to be positive on the top part of the blade when the tip vortex is undergoing its roll-up process.

C. Turbulence Characteristics

A detailed analysis was performed on the measured turbulence characteristics to help understand the evolutionary behavior of the tip vortices. In this case, 1000 velocity vector maps were used to estimate the fluctuating velocity components, which is sufficient to ensure statistical convergence. Notice that all of the first- and second-order velocity fluctuations were normalized by V_{tip}, and V_{tip}^2, respectively, and the length scale was normalized by the blade radius R.

1. *Turbulence Intensities*

Figure 15 shows the distribution of normalized turbulence intensities U_{rms} and V_{rms} from $\zeta = -4$ deg ($\approx$33%c from the leading edge of the blade) to 4 deg wake age ($\approx$66%c from the leading edge of the blade). The solid black area represents the thickness of the

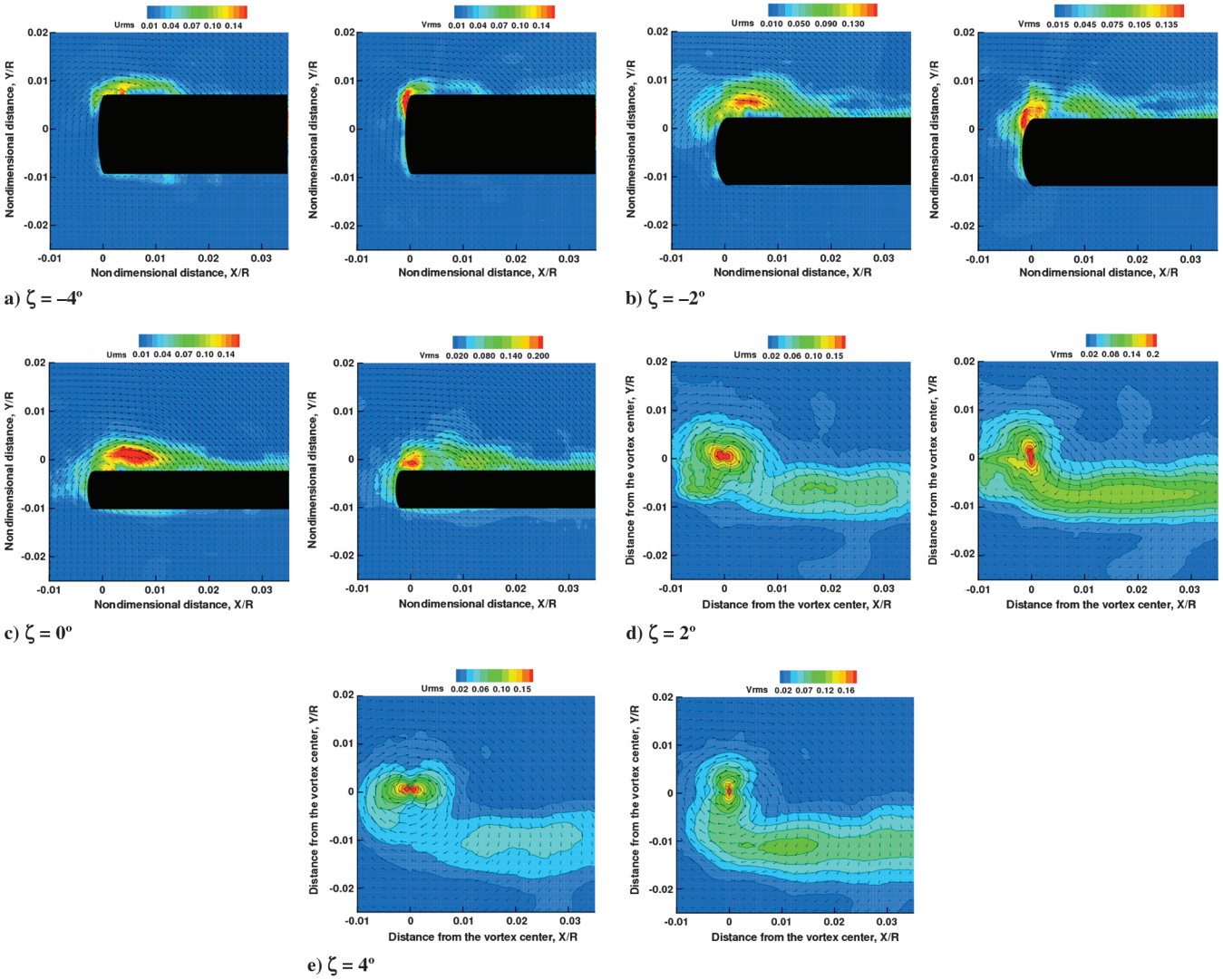

Fig. 15 In-plane measurements of turbulence intensities during the tip vortex roll up over 8 deg of wake age. Every third vector has been plotted to prevent image congestion.

blade. It can be seen from Figs. 15d and 15e that U_{rms} and V_{rms} are aligned along the x and y axes, respectively. This alignment also occurs in the initial stages of the roll up (i.e., at $\zeta = -2$ deg) and correlates with the previous turbulence measurements made using 2-C PIV [51] and also with those made behind a fixed wing [53,54]. Although the alignment pattern remains the same at all wake ages, its magnitude varies with wake age.

Figure 16 shows the distribution of turbulence that was obtained by making a horizontal cut across the centerline of the tip vortex at 2 deg of wake age. Along the horizontal cut, the Cartesian components of the velocity U_{rms} and V_{rms} will be equivalent to the $V_{r\,\text{rms}}$ and $V_{\theta\,\text{rms}}$ components in polar coordinates, respectively. Because of the alignment in the U_{rms} component (i.e., $V_{r\,\text{rms}}$ in this case) along the horizontal cut, the $V_{r\,\text{rms}}$ distribution is noticeably wider than for the $V_{\theta\,\text{rms}}$ distribution.

Furthermore, it was found that both turbulence intensities reached a maximum at the vortex center. This can be seen from the contours shown in Fig. 17. Furthermore, it can also be seen that $V_{r\,\text{rms}} > V_{\theta\,\text{rms}}$. This observation is of particular significance in understanding the structure of tip vortices and has been used by Chow et al. [54] to explain the turbulence intensity alignment that was shown in Fig. 15.

Examining the turbulence production terms for $V_{r\,\text{rms}}$ and $V_{\theta\,\text{rms}}$ transport shows that

$$V'_{r(\text{prod})} = -2\left[\bar{V}'^2_r \frac{\partial V_r}{\partial r} + \overline{V'_z V'_r}\frac{\partial V_r}{\partial z} - \frac{V_\theta}{r}\overline{V'_r V'_\theta}\right] \tag{6}$$

and

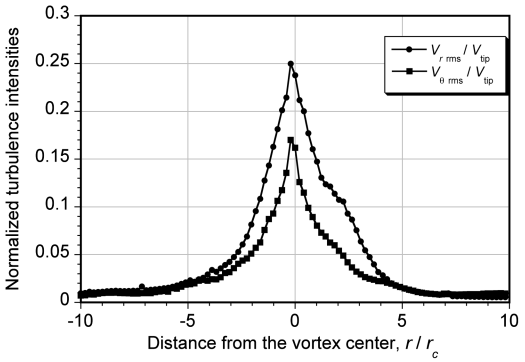

Fig. 16 Turbulence intensity distribution across the blade tip vortex at 2 deg of wake age.

$$V'_{\theta(\text{prod})} = -2\left[\bar{V}'^2_\theta \frac{\partial V_r}{\partial r} + \overline{V'_z V'_\theta}\frac{\partial V_\theta}{\partial z} + \frac{\partial V_\theta}{\partial r}\overline{V'_r V'_\theta}\right] \tag{7}$$

Comparing these two equations, it is seen that the second term is the streamwise gradient of the in-plane velocities. This term is relatively small and becomes even smaller when multiplied by shear stress. The velocity gradient in the first term is very small, mainly because the radial velocity is small, therefore the gradient of radial velocity becomes even smaller. However, the presence of a normal stress term (which is usually significantly larger than the shear stresses) does tend to compensate for the small gradients found in the radial velocity.

The last term in both Eqs. (6) and (7) involves the shear stress and the swirl velocity gradients. Inside the vortex cores, the components V_θ/r and $\partial V_\theta/\partial r$ are very similar in magnitude. The significance here, however, is the sign of the last term in the equations. Although this term is negative for the V'_r term, it is positive for the V'_θ term. Whereas $V'_r V'_\theta$ is usually assumed to be zero for solid body rotation, the present results show its value to be predominantly negative. A nonzero value of $V'_r V'_\theta$ will, therefore, increase the production of $V_{r\,\text{rms}}$ and reduce $V_{\theta\,\text{rms}}$, resulting in the $V_{r\,\text{rms}}$ component being greater than the $V_{\theta\,\text{rms}}$ component. This result, in turn, explains the reason behind the turbulence intensity pattern alignment observed in the U_{rms} and V_{rms} components, as shown previously in Fig. 15.

Figures 18a and 18b compare the turbulence intensities measured across the tip vortex at 30 deg of wake age as obtained using PIV and LDV. Good correlation can be seen, even though the LDV measurements in this case have not been corrected for aperiodicity bias. Although procedures are available to correct the peak swirl velocity and core size when making LDV measurements [55], no such procedures have yet been established for turbulence measurements. However, at early wake ages, the magnitude of the aperiodicity in the flow is relatively low and allows such a comparison to be conducted with good confidence.

2. *Reynolds Stresses*

Figure 19 shows the distribution of Reynolds shear stress ($\overline{u'v'}$) and the associated strain ($\partial u/\partial y + \partial v/\partial x$) measured from a wake age of $\zeta = -4$ deg (on the blade) to $\zeta = 4$ deg (in the wake). The reason to show shear stress and strain together stems directly from the basic assumption made in linear eddy viscosity-based turbulence models that stress is represented as a linear function of strain. However, even a cursory examination of the contours in Fig. 19 clearly suggests that this assumption is invalid, as has already been shown for curved streamlines [33,56]. This result seems to be true regardless of the wake age.

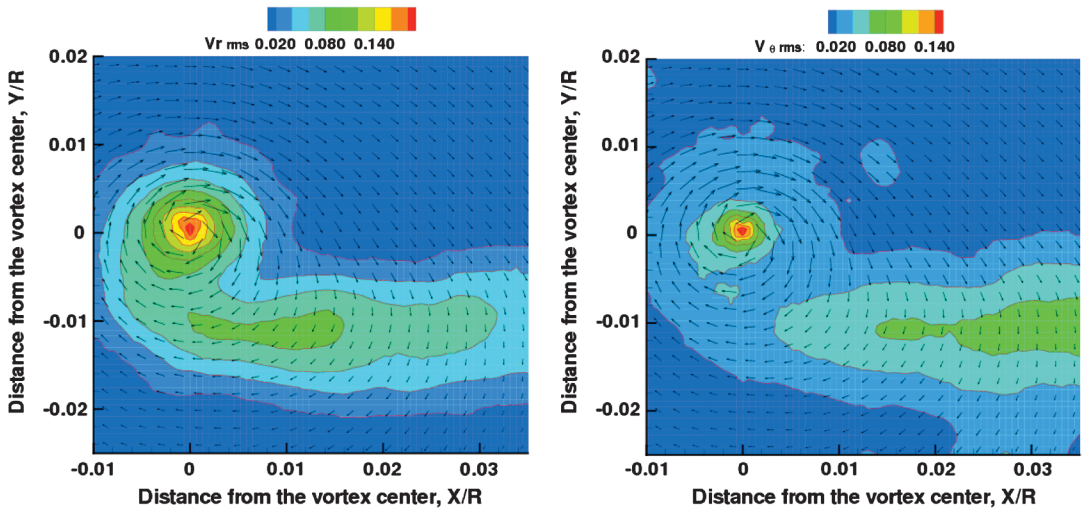

a) $V_{r\,\text{rms}}$ b) $V_{\theta\,\text{rms}}$

Fig. 17 Turbulence intensity distribution (in polar coordinates) in the tip vortex at $\zeta = 4$ deg of wake age.

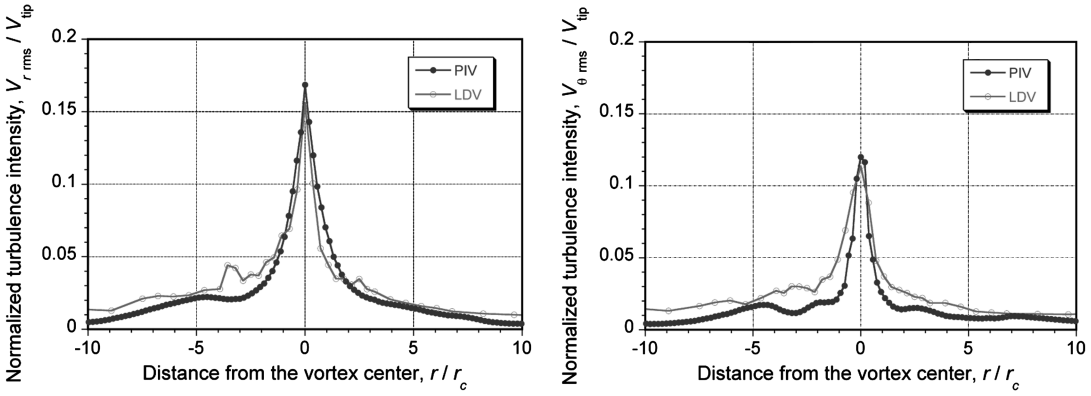

a) $V_{r\,\mathrm{rms}}$ b) $V_{\theta\,\mathrm{rms}}$

Fig. 18 Comparison of turbulence measurements using PIV and LDV showing a) $\overline{Vr'}$, and b) $\bar{V}'_\theta$.

Figure 19 shows that the magnitude of both the shear stress and strain continue to change with wake age and eventually form a clear four-lobbed pattern as early as $\zeta = 2$ deg. These lobes, of which magnitudes alternate in sign, are aligned along the Cartesian coordinate axes for strain and at 45 deg with respect to the coordinate axes for the shear stress. The contours also suggest significantly high levels of shear stress inside the vortex sheet at early wake ages, which can be expected based on the instantaneous turbulence activity that has been shown previously in Fig. 8.

Figures 20 and 21 show the Reynolds shear stress component (i.e., $\overline{u'v'}$) and its associated strain (i.e., $\partial u/\partial y + \partial v/\partial x$) for the fully developed tip vortex at 60 deg of wake age. The results in this figure also include the stress and strain contours from a vortex flow produced by a microrotor [51]. Excellent correlation can be seen

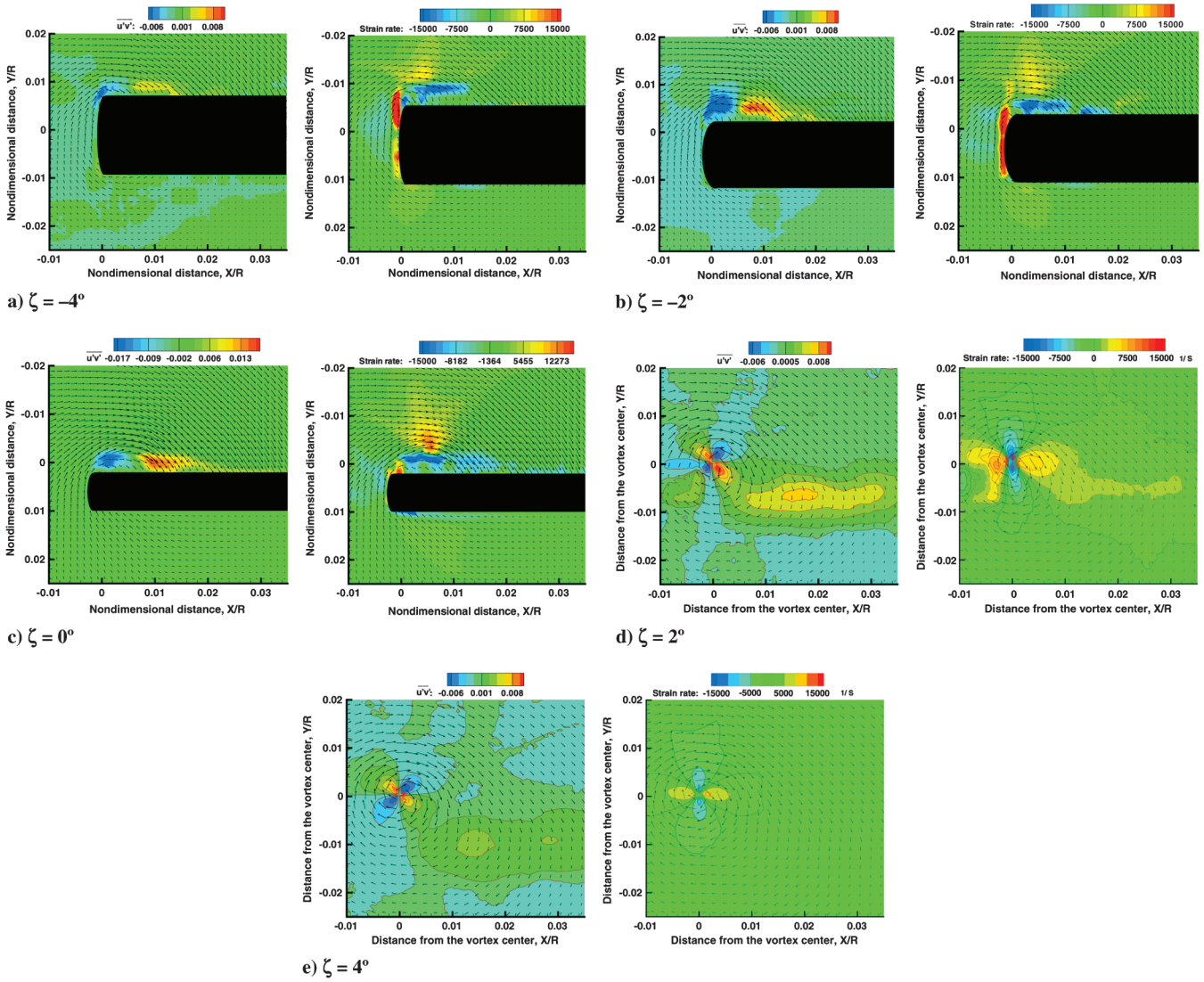

a) $\zeta = -4°$ b) $\zeta = -2°$

c) $\zeta = 0°$ d) $\zeta = 2°$

e) $\zeta = 4°$

Fig. 19 Reynolds shear stress (left column) and strain (right column) at various wake ages.

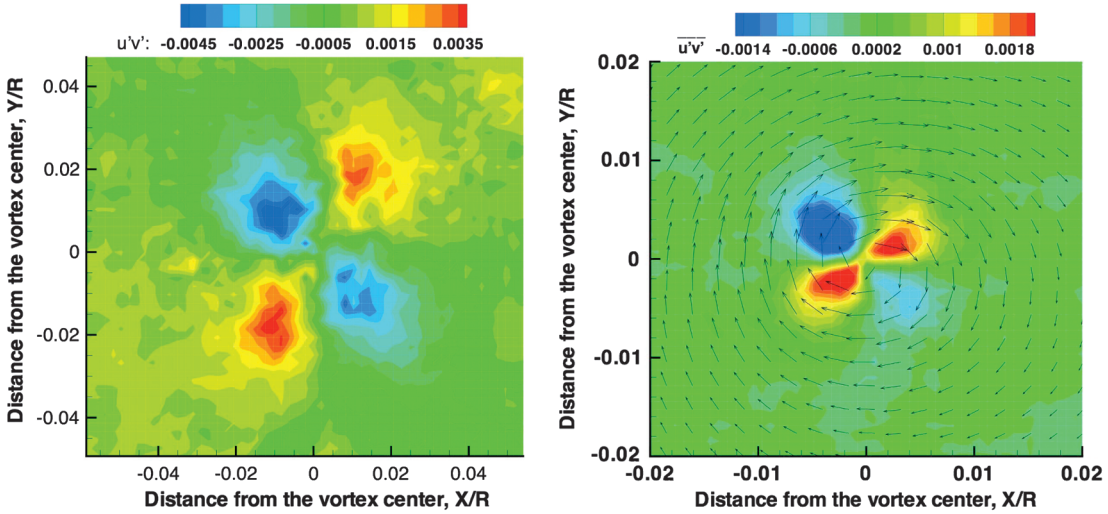

a) Ramasamy et al. [38] b) Present measurements

Fig. 20 Reynolds shear stresses $\overline{u'v'}$ at 60 deg wake age.

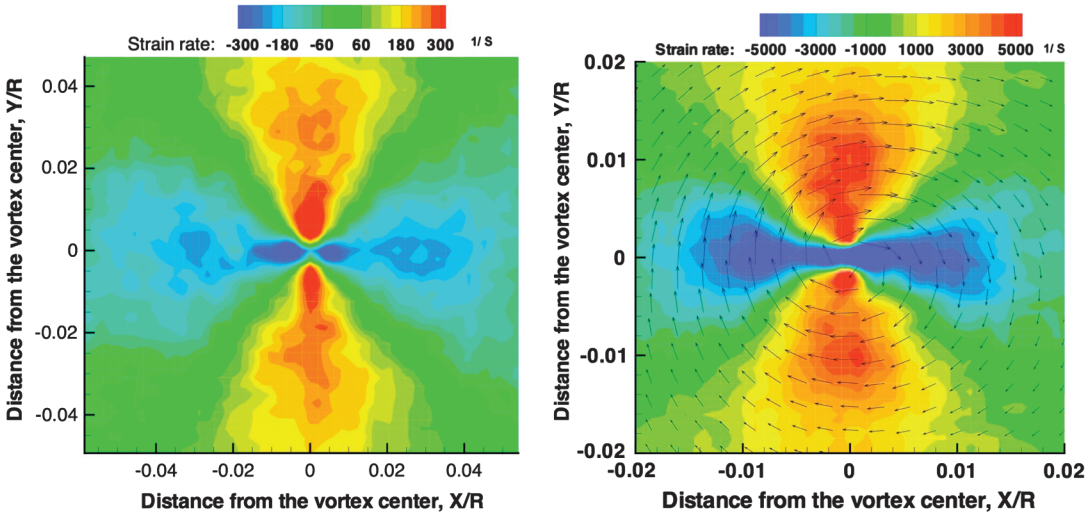

a) Ramasamy et al. [38] b) Present measurements

Fig. 21 Reynolds shear strain rate $-(\frac{\partial u}{\partial y}+\frac{\partial v}{\partial x})$ at 60 deg wake age.

between the two sets of results. Both of these results were also found to correlate well with the turbulence measurements made by Chow et al. [54] on a fixed wing tested in a wind tunnel (and at higher chord and vortex Reynolds numbers).

Figure 22 shows a similar plot for the $\overline{v'w'}$ component of the Reynolds shear stress and its associated strain. Unlike the $\overline{u'v'}$ term, the $\overline{v'w'}$ term has only two lobes. These measurements were also found to correlate well with the turbulence measurements made by Chow et al. [54]. However, the alignment of the lobes are still 45 deg offset from the coordinate axes. The associated strain also shows only two lobes, which are aligned with the x axis. This suggests that the orientation of all the shear stress distributions are 45 deg offset from the shear strain distribution, a result that is most likely independent of the vortex Reynolds number.

The importance of the $\overline{v'w'}$ term, which is the correlation term between the streamwise and the crossflow directions, can be better understood from the momentum equation in the z direction, which is given by

$$u\frac{\partial u}{\partial z}+v\frac{\partial v}{\partial z}+w\frac{\partial w}{\partial z}=-\frac{1}{\rho}\frac{\partial p}{\partial z}+\nu\nabla^2 w-\frac{\partial \overline{u'w'}}{\partial x}-\frac{\partial \overline{v'w'}}{\partial y}-\frac{\partial \bar{w}'^2}{\partial z} \tag{8}$$

The pressure gradient in Eq. (8), which is positive during the tip vortex roll up (resulting in increased axial velocity deficit as the wake age increases), can be assumed negligible at older wake ages. Similarly, the effects of molecular viscosity alone can be considered negligible compared with the effects of the turbulent (eddy) viscosity. This leaves the gradients of the stress terms (i.e., $\overline{u'w'}$, $\overline{v'w'}$, and $\bar{w}'^2$) to play a role in defining the axial momentum in a vortex flow. This will be especially important at the centerline of the vortex, where the axial velocity deficit is at a maximum.

The results in Fig. 22b suggests that the gradient $\partial\overline{v'w'}/\partial y$ is very high inside the vortex core. Such high gradients directly transfer momentum from the streamwise direction to the crossflow direction, resulting in the reduction of the peak axial velocity, as shown in Fig. 12b. A simple way to correlate the growth rate of the tip vortex (Fig. 13) and the production of turbulence is through comparisons of the distributions of the eddy viscosity across the vortex core. The vortex core growth depends on the diffusion of momentum from one layer in the fluid to another. This diffusion depends on the eddy viscosity, which in turn is a function of the shear stress (i.e., Boussinesq's assumption).

Figure 23 shows the measured Reynolds shear stress $\overline{u'v'}$ in the tip vortex for three wake ages. It is clear that the peak value of the shear

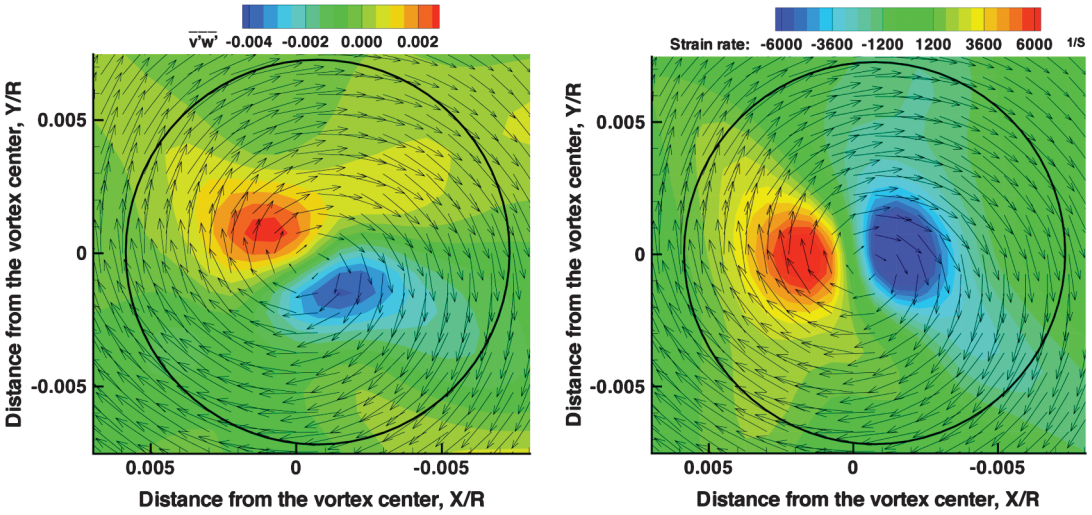

a) Shear stress b) Strain rate

Fig. 22 Reynolds stress ($\overline{v'w'}$) and strain rate $\frac{\partial v}{\partial z} + \frac{\partial w}{\partial y}$ at 60 deg wake age showing anisotropy.

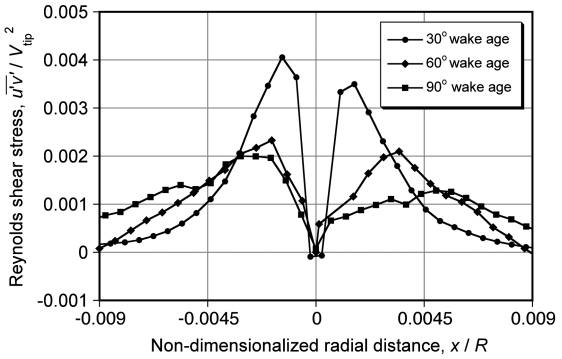

Fig. 23 Measured Reynolds shear stress $\overline{u'v'}$ in the tip vortex for three wake ages.

stress decreases with wake age and is distributed further away from the vortex center. Although the peak values of shear stress move radially further away from the core at the older ages, it can also be seen that the area under the curves remains approximately constant. This means that average eddy viscosity is also approximately constant, which is the basic assumption made in Squire's core growth model [52]. The existence of the shear stress is the basic phenomenon that will sustain the growth rate of the vortex cores.

Notice that the eddy or turbulent viscosity can be modeled as

$$-\overline{u'v'} = \frac{\tau}{\rho} = \nu_\tau |\sigma| \tag{9}$$

The R–L turbulence model [32] (outlined previously) is based on a Richardson number (Ri) concept, which is the ratio of turbulence produced or consumed as a result of centrifugal force to turbulence produced from shear [33]. Turbulence produced from shear is usually very low at the center of the vortex (pure solid bodylike rotation does not produce any turbulence). As a result, the value of Ri is high near the center of the vortex and much larger than the threshold value that allows for turbulence (see Fig. 2). Therefore, no turbulence is produced near the center of a vortex, a result suggested previously in the flow visualization results of Fig. 1.

The momentum transfer across the layers of fluid inside the tip vortex core depends largely on the shear stress. Because it has been shown in Fig. 23 that the shear stress reaches a minimum at the vortex center, the VIF used in the R–L turbulence model is, therefore, consistent with the findings made in the present set of measurements.

V. Conclusions

Comprehensive measurements in the flowfield of a hovering rotor were performed using dual-plane stereoscopic particle image velocimetry. This DPS–PIV technique allowed for the measurement of all three flow velocities and also all nine components of the velocity gradient tensor, a capability not possible with conventional or "classical" PIV. The DPS–PIV method was based on coincident PIV measurements made over two differentially spaced laser sheet planes. A polarization-based approach was used in which the two laser sheets were given orthogonal polarizations, with filters and beam-splitting optical cubes placed so that the imaging cameras saw Mie scattering from only one or other of the laser sheets. The digital processing of the acquired images was based on a deformation grid correlation algorithm optimized for the high velocity gradient and turbulent flows found in blade tip vortices. The measurements discussed in this paper have concentrated on the vortex wake system behind the blade and examined the tip vortex evolution from as early as $\zeta = -4$ deg (on the top, side edge, and bottom of the blade) to about 270 deg of wake age downstream.

The following are the specific conclusions drawn from this study:

1) High-resolution imaging of the inner vortex sheet trailing behind the rotor blade revealed the presence of several counter-rotating Taylor–Görtler vortices. These vortices seem to be responsible for producing substantial turbulence in the initial flow properties of the rolled-up tip vortices. These fluctuations, combined with the high velocity gradients found in these vortices, play a significant role in the momentum transfer properties.

2) Excellent quantitative correlation was found between the LDV and PIV measurements of turbulence, confirming that PIV can be confidently applied to make turbulence measurements. The use of 1000 PIV samples was found to be sufficient based on a comparison of the results obtained with 20,000 samples obtained during the LDV measurements. This establishes the sample size requirement to establish the sample size requirement for the statistical convergence of turbulence measurements made inside the tip vortices when using PIV.

3) The mean characteristics of the tip vortices, such as their core size, peak swirl velocity, and their variation with time, were found to correlate well with measurements made using LDV. The radial diffusion of vorticity from turbulence generation was found to be about eight times higher than that obtained using a laminar assumption. The measured peak axial velocity deficit (corrected for aperiodicity bias effects) was found to be about 75% of the tip speed at the earliest wake age behind the blade. This reduced to only 40% at 60 deg of wake age.

4) Turbulence intensity measurements inside the tip vorticies clearly showed a significant anisotropy. Specifically, the $V_{r\,\mathrm{rms}}$ component was greater in magnitude than the $V_{\theta\,\mathrm{rms}}$ component in

both the near and far wake. The very presence of the $\overline{V_r' V_\theta'}$ term (which is typically assumed to be zero for solid body-like flow rotation) can be concluded as the primary reason for this anisotropy.

5) Good correlation was found in the Reynolds shear stress distributions and strain rates between the present measurements and earlier published measurements made on a fixed wing. This suggests that the turbulence pattern probably remains essentially the same for all tip vortices, regardless of the operating Reynolds number or the type of lifting surface from which they were generated. The results also confirm that shear stresses cannot be written as a linear function of strain, as assumed in existing linear eddy viscosity-based turbulence models.

Acknowledgments

This research was partly supported by the Army Research Office (ARO) under grant W911NF0610394 and partly under the Multi-University Research Initiative under grant W911NF0410176. Thomas Doligalski was the technical monitor for both contracts. The authors would also like to acknowledge the University Affiliated Research Center for paying part of the printing charges. The authors would like to thank Christopher Cadou and Kenneth Yu for loaning the additional lasers needed for this work. Our appreciation extends also to Joseph Ramsey, who aided in the data reduction and analysis.

References

[1] Drees, J. M., and Hendal, W. P., "The Field of Flow Through a Helicopter Rotor Obtained from Wind Tunnel Smoke Tests," *Journal of Aircraft Engineering*, Vol. 23, No. 266, Feb. 1950, pp. 107–111.

[2] Landgrebe, A. J., "An Analytical Method for Predicting Rotor Wake Geometry," *The AIAA/AHS VTOL Research, Design & Operations Meeting*, AIAA, New York, Feb. 1969, pp. 20–32.

[3] Cook, C. V., "The Structure of the Rotor Blade Tip Vortex," *Aerodynamics of Rotary Wings*, AGARD, Rept. CP-111, Sept. 1972.

[4] Tung, C., Pucci, S. L., Caradonna, F. X., and Morse, H. A., "The Structure of Trailing Vortices Generated by Model Helicopter Rotor Blades," NASA TM 81316, 1981.

[5] Egolf, T. A., and Landgrebe, A. J., "Helicopter Rotor Wake Geometry and its Influence in Forward Flight," *Generalized Wake Geometry and Wake Effects in Rotor Airloads and Performance*, Vol. 1, NASA CR-3726, Oct. 1983.

[6] Johnson, W., "Wake Model for Helicopter Rotors in High Speed Flight," NASA CR-1177507, Nov. 1988; also U.S. Army Aviation Systems Command TR-88-A-008.

[7] Leishman, J. G., and Bi, N., "Measurements of a Rotor Flowfield and the Effects on a Body in Forward Flight," *Vertica*, Vol. 14, No. 3, 1990, pp. 401–415.

[8] Lorber, P. F., Stauter, R. C., Pollack, M. J., and Landgrebe, A. J., "A Comprehensive Hover Test of the Airloads and Airflow of an Extensively Instrumented Model Helicopter Rotor," U.S. Army Aviation Systems Command TR-D-16 (A-E), Vols. 1–5, Oct. 1991.

[9] Bagai, A., Moedersheim, E., and Leishman, J. G., "Developments in the Visualization of Rotor Wakes Using the Wide-Field Shadowgraph Method," *Journal of Flow Visualization and Image Processing*, Vol. 1, No. 3, July–Sept. 1993, pp. 211–233.

[10] Bhagwat, M. J., and Leishman, J. G., "Stability Analysis of Helicopter Rotor Wakes in Axial Flight," *Journal of the American Helicopter Society*, Vol. 45, No. 3, July 2000, pp. 165–178. doi:10.4050/JAHS.45.165

[11] Bagai, A., and Leishman, J. G., "Flow Visualization of Compressible Vortex Structures Using Density Gradient Techniques," *Experiments in Fluids*, Vol. 15, No. 6, Oct. 1993, pp. 431–442.

[12] McAlister, K. W., "Measurements in the Near Wake of a Hovering Rotor," *Proceedings of the 27th AIAA Fluid Dynamics Conference*, AIAA Paper 96-1958, New Orleans, LA, June 1996.

[13] Caradonna, F., Hendley, E., Silva, M., Huang, S., Komerath, N., Reddy, U., Mahalingam, R., Funk, R., Wong, O., Ames, R., Darden, L., Villareal, L., and Gregory, J., "An Experimental Study of a Rotor in Axial Flight," *Proceedings of the AHS Technical Specialists' Meeting for Rotorcraft Acoustics and Aerodynamics*, American Helicopter Society International, Alexandria, VA, Oct. 1997.

[14] Leishman, J. G., Han, Y. O., and Coyne, A. J., "Measurements of the Velocity and Turbulence Structure of a Rotor Tip Vortex," *AIAA Journal*, Vol. 35, No. 3, March 1997, pp. 477–485. doi:10.2514/2.120

[15] Mahalingam, R., and Komerath, N. M., "Measurements of the Near Wake of a Rotor in Forward Flight," *36th Aerospace Sciences Meeting & Exhibit*, AIAA Paper 98-0692, Reno, NV, Jan. 1998.

[16] Martin, P. B., and Leishman, J. G., "Trailing Vortex Measurements in the Wake of a Hovering Rotor with Various Tip Shapes," *Proceedings of the American Helicopter Society 58th Annual National Forum*, American Helicopter Society International, Alexandria, VA, July 2002.

[17] Ramasamy, M., and Leishman, J. G., "Interdependence of Diffusion and Straining of Helicopter Blade Tip Vortices," *Journal of Aircraft*, Vol. 41, No. 5, Sept. 2004, pp. 1014–1024. doi:10.2514/1.3364

[18] Bhagwat, M. J., and Leishman, J. G., "Correlation of Helicopter Tip Vortex Measurements," *AIAA Journal*, Vol. 38, No. 2, Feb. 2000, pp. 301–308. doi:10.2514/2.957

[19] Bhagwat, M. J., and Leishman, J. G., "Measurements of Bound and Wake Circulation on a Helicopter Rotor," *Journal of Aircraft*, Vol. 37, No. 2, 2000, pp. 227–234. doi:10.2514/2.2611

[20] Johnson, W., "Rotorcraft Aerodynamics Models for a Comprehensive Analysis," *Proceedings of the American Helicopter Society 54th Annual National Forum*, American Helicopter Society International, Alexandria, VA, May 1998.

[21] Datta, A., and Chopra, I., "Validation and Understanding of UH-60 Vibratory Loads in Steady Level Flight," *Journal of the American Helicopter Society*, Vol. 49, No. 3, July 2004, pp. 271–287. doi:10.4050/JAHS.49.271

[22] Johnson, D. A., and King, L. S., "A Mathematically Simple Turbulence Closure Model for Attached and Separated Turbulent Boundary Layers," *AIAA Journal*, Vol. 23, No. 11, 1985, pp. 1684–1692. doi:10.2514/3.9152

[23] Durbin, P. A., "Near-Wall Turbulence Closure Modelling Without Damping Functions," *Theoretical and Computational Fluid Dynamics*, Vol. 3, No. 1, 1991, pp. 1–13.

[24] Baldwin, B. S., and Lomax, P. S., "Thin Layer Approximation and Algebraic Model for Separated Turbulent Flows," *16th AIAA Aerospace Sciences Meeting and Exhibit*, AIAA Paper 78-0257, Huntsville, AL, Jan. 1978.

[25] Spalart, P. R., and Allmaras, S. R., "A One-Equation Turbulence Model for Aerodynamic Flows," *30th AIAA Aerospace Sciences Meeting & Exhibit*, AIAA Paper 92-0439, Jan. 1992.

[26] Baldwin, B. S., and Barth, T. J., "A One Equation Turbulence Transport Model for High Reynolds Number Wall Bounded Flows," NASA TM 102847, Aug. 1990.

[27] Petterson, R., "A Non-Linear Eddy Viscosity Model for Near-Wall Turbulence," *38th AIAA Aerospace Sciences Meeting & Exhibit*, AIAA Paper 00-0135, Reno, NV, Jan. 2000.

[28] Dacles–Mariani, J., Zilliac, G. G., Chow, J. S., and Bradshaw, P., "Numerical/Experimental Study of a Wing Tip Vortex in the Near Field," *AIAA Journal*, Vol. 33, No. 9, 1995, pp. 1561–1568. doi:10.2514/3.12826

[29] Van Driest, E. R., "Turbulence Boundary Layer in a Compressible Fluids," *Journal of the Aeronautical Sciences*, Vol. 18, No. 3, 1951, pp. 145–160.

[30] Van Driest, E. R., "On Turbulence Flow Near A Wall," *Journal of the Aeronautical Sciences*, Vol. 23, No. 11, 1956, pp. 1007–1011.

[31] Klebanoff, P. S., "Characteristics of Turbulence in a Boundary Layer with Zero Pressure Gradient," NACA TN 3178, 1956.

[32] Ramasamy, M., and Leishman, J. G., "A Generalized Model for Transitional Blade Tip Vortices," *Journal of the American Helicopter Society*, Vol. 51, No. 1, Jan. 2006, pp. 92–103. doi:10.4050/1.3092881

[33] Bradshaw, P., "The Analogy Between Streamline Curvature and Buoyancy in Turbulent Shear Flows," *Journal of Fluid Mechanics*, Vol. 36, No. 1, March 1969, pp. 177–191. doi:10.1017/S0022112069001583

[34] Duraisamy, K., Ramasamy, M., Baeder, J. D., and Leishman, J. G., "High Resolution Computational and Experimental Study of Rotary Wing Tip Vortex Formation," *AIAA Journal*, Vol. 45, No. 11, Nov. 2007, pp. 2593–2602. doi:10.2514/1.26575

[35] Leishman, J. G., "On Seed Particle Dynamics in Tip Vortex Flows," *Journal of Aircraft*, Vol. 33, No. 4, July/Aug. 1996, pp. 823–825. doi:10.2514/3.47020

[36] Martin, P. B., Bhagwat, M. J., and Leishman, J. G., "Strobed Laser-Sheet Visualization of a Helicopter Rotor Wake," *Proceedings of PSFVIP-2*, Paper PF118, Honolulu, HI, May 1999.

[37] Bhagwat, M. J., and Leishman, J. G., "On the Stability of the Wake of a

Rotor in Axial Flight," *Proceedings of the American Helicopter Society 56th Annual National Forum*, American Helicopter Society International, Alexandria, VA, May 2000.

[38] Ramasamy, M., Johnson, B., Huismann, T., and Leishman, J. G., "A New Method for Estimating Turbulent Vortex Flow Properties from Stereoscopic DPIV Measurements," *Proceedings of the American Helicopter Society 63rd Annual National Forum*, American Helicopter Society International, Alexandria, VA, May 2007.

[39] Raffel, M., Richard, H., Ehrenfried, K., van der Wall, B. G., Burley, C. L., Beaumier, P., McAlister, K. W., and Pengel, K., "Recording and Evaluation Methods of PIV Investigations on a Helicopter Rotor Model," *Experiments in Fluids*, Vol. 36, No. 1, 2004, pp. 146–156. doi:10.1007/s00348-003-0689-7

[40] Heineck, J. T., Yamauchi, G. K., Wadcock, A. J., Lourenco, L., and Abrego, A. I., "Application of Three-Component PIV to a Hovering Rotor Wake," *Proceedings of the American Helicopter Society 56th Annual National Forum*, American Helicopter Society International, Alexandria, VA, May 2000.

[41] van der Wall, B. G., and Richard, H., "Analysis Methodology for 3C-PIV Data of Rotary Wing Vortices," *Experiments in Fluids*, Vol. 40, No. 5, May 2006, pp. 798–812. doi:10.1007/s00348-006-0117-x

[42] Mullin, J. A., and Dahm, W. J. A., "Dual-Plane Stereo Particle Image Velocimetry (DSPIV) for Measuring Velocity Gradient Fields at Intermediate and Small Scales of Turbulent Flows," *Experiments in Fluids*, Vol. 38, No. 2, Feb. 2005, pp. 185–196. doi:10.1007/s00348-004-0898-8

[43] Hu, H., Saga, T., Kobayashi, N., Taniguchi, N., and Yasuki, M., "Dual-Plane Stereoscopic Particle Image Velocimetry: System Setup and its Application On a Lobed Jet Mixing Flow," *Experiments in Fluids*, Vol. 31, No. 3, Sept. 2001, pp. 277–293. doi:10.1007/s003480100283

[44] Ganapathisubramani, B., Longmire, E. K., Marusic, I., and Stamatios, P., "Dual-Plane PIV Technique to Determine the Complete Velocity Gradient Tensor in a Turbulent Boundary Layer," *Experiments in Fluids*, Vol. 39, No. 2, Aug. 2005, pp. 222–231. doi:10.1007/s00348-005-1019-z

[45] Scarano, F., "Iterative Image Deformation Methods in PIV," *Measurement Science and Technology*, Vol. 13, No. 1, 2002, pp. R1–R19. doi:10.1088/0957-0233/13/1/201

[46] Ramasamy, M., and Leishman, J. G., "Benchmarking Particle Image Velocimetry with Laser Doppler Velocimetry for Rotor Wake Measurements," *AIAA Journal*, Vol. 45, No. 11, Nov. 2007, pp. 2622–2633. doi:10.2514/1.28130

[47] Martin, P. B., Pugliese, G., and Leishman, J. G., "Laser Doppler Velocimetry Uncertainty Analysis for Rotor Blade Tip Vortex Measurements," *38th AIAA Aerospace Sciences Meeting and Exhibit*, AIAA CP 2000-0063, Reno, NV, Jan. 2000.

[48] Hall, P., "Taylor–Gortler Vortices in Fully Developed Boundary Layer Flows," *Journal of Fluid Mechanics*, Vol. 124, 1982, pp. 475–494. doi:10.1017/S0022112082002596

[49] Momayez, L., Dupont, P., and Peerhossaini, H., "Effects of Vortex Organization on Heat Transfer Enhancement," *International Journal of Thermal Sciences*, Vol. 43, No. 8, Aug. 2004, pp. 753–760. doi:10.1016/j.ijthermalsci.2004.02.015

[50] Tangler, J. L., Wohlfeld, R. M., and Miley, S. J., "An Experimental Investigation of Vortex Stability, Tip Shapes, Compressibility, and Noise for Hovering Model Rotors," NASA CR-2305, Sept. 1973.

[51] Ramasamy, M., Leishman, J. G., and Lee, T. E., "Flowfield of a Rotating Wing MAV," *Journal of Aircraft*, Vol. 44, No. 4, July 2007, pp. 1236–1244. doi:10.2514/1.26415

[52] Squire, H. B., "The Growth of a Vortex In Turbulent Flow," *Aeronautical Quarterly*, Vol. 16, No. Aug. 1965, pp. 302–306.

[53] Chow, J. S., Zilliac, G. G., and Bradshaw, P., "Measurements in the Near-Field of a Turbulent Wingtip Vortex," *31st Aerospace Sciences Meeting & Exhibit*, AIAA Paper 93-0551, Jan. 1993.

[54] Chow, J. S., Zilliac, G. G., and Bradshaw, P., "Mean and Turbulence Measurements in the Near Field of a Wingtip Vortex," *AIAA Journal*, Vol. 35, No. 10, Oct. 1997, pp. 1561–1568. doi:10.2514/2.1

[55] Leishman, J. G., "Measurements of the Aperiodic Wake of a Hovering Rotor," *Experiments in Fluids*, Vol. 25, No. 4, 1998, pp. 352–361. doi:10.1007/s003480050240

[56] Zilliac, G. G., Chow, J. S., Dacles–Mariani, J., and Bradshaw, P., "Turbulent Structure of a Wingtip Vortex in the Near Field," *Proceedings of the 24th AIAA Fluid Dynamic Conference*, AIAA Paper 93-3011, July 1993.

[57] Martin, P. B., Pugliese, G., and Leishman, J. G., "High Resolution Trailing Vortex Measurements in the Wake of a Hovering Rotor," *Proceedings of the American Helicopter Society 57th Annual National Forum*, American Helicopter Society International, Alexandria, VA, May 2001.

R. Lucht
Associate Editor